

Simulation of AGNs for eROSITA

Bachelorarbeit

vorgelegt von
Thorsten Brand

Erlangen Centre for Astroparticle Physics
Dr. Karl Remeis-Sternwarte Bamberg
Friedrich-Alexander-Universität
Erlangen-Nürnberg

1. Gutachter: Prof. Dr. Jörn Wilms
2. Gutachter: Prof. Dr. Ulrich Heber

Tag der Abgabe: 02.08.2011

Abstract

In this Bachelor's thesis a simulation of the Cosmic X-Ray Background (CXRB) which consists of a large number of Active Galactic Nuclei (AGN) is presented. It provides source catalogs in SIMPUT-style for observation simulations, e.g. for the German multi-mirror telescope eROSITA aboard the Russian satellite *Spectrum Roentgen-Gamma*. The scientific background is discussed as well as the program structure. As few source intrinsic parameters as possible are simulated, but observed distributions such as the $\log(N(> S)) - \log(S)$ -distribution are focused. This non-source-intrinsic simulation approach results in difficulties to create a realistic sample because of missing data about relations between the physical parameters flux S , column density N_{H} and redshift z . However, by adjusting the distribution parameters useful and overall physically reasonable source catalogs can be generated. Their properties are compared to real data as well as to relevant models. Pictures of simulated observations on these sources performed by Christian Schmid are presented additionally.

Contents

1	Introduction	5
1.1	The eROSITA telescope	5
1.2	Simulations for eROSITA	8
2	The Cosmic X-Ray Background	9
2.1	The X-Ray Background	9
2.2	Properties of AGN	10
2.3	Properties of the Cosmic X-Ray Background	11
3	Simulation of the Cosmic X-Ray Background	14
3.1	Simulation objective	14
3.2	Program structure	14
3.3	Parameter input	15
3.4	Random source generation	16
3.4.1	Source positions	16
3.4.2	Source fluxes	17
3.4.3	Redshift distribution	19
3.4.4	Spectral indices	20
3.4.5	Column densities	20
3.4.6	Grids and source catalog	22
3.5	Generation of spectra	22
3.6	Comparison of the simulated XRB to real data	24
4	First results of simulated observations	30
5	Conclusions	32

Chapter 1

Introduction

In this paper a simulation approach on the Cosmic X-Ray Background for further observation simulations is presented.

First, the instrument for which this work has been done is presented and the main simulation is introduced in Chapter 1. Then, the physical foundation for the simulation is discussed in Chapter 2. Afterwards, the actual program is described in detail in Chapter 3. Example images from a simulated observation are shown in Chapter 4.

1.1 The eROSITA telescope

eROSITA (extended ROentgen Survey with an Imaging Telescope Array) is a German multi-mirror space telescope project sensitive for X-Ray photons. Together with the Russian Astronomical Roentgen Telescope (ART) it will be one of two instruments aboard the Russian satellite *Spectrum Roentgen-Gamma* (SRG, Fig. 1.1) which will be launched in late 2013 from Baikonur. It will map the whole sky at energies between 0.2 keV and 12 keV (Predehl et al. 2006).

eROSITA's optics consist of seven Wolter-I mirror modules with 54 shells each. They all have

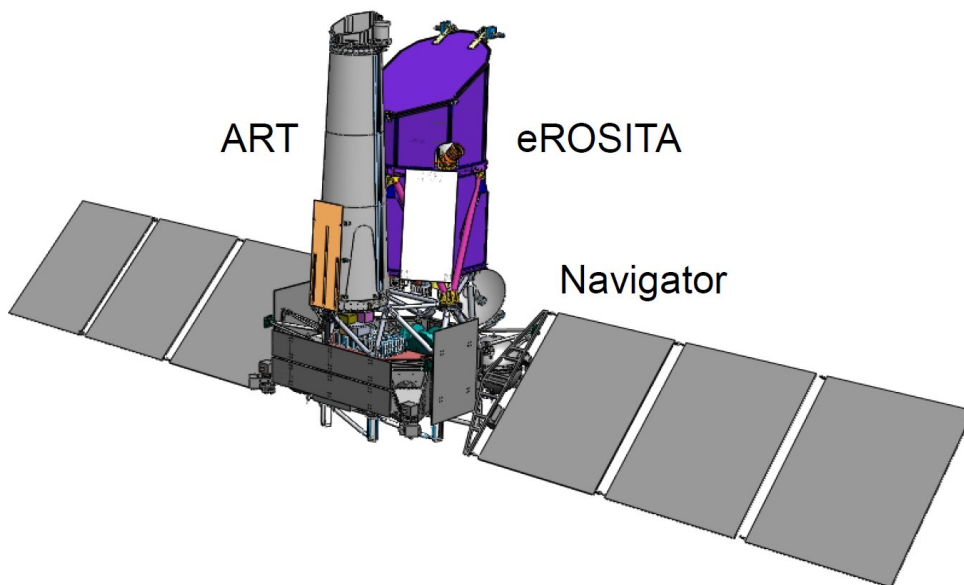


Figure 1.1: *The SXG-Satellite with the two instruments eROSITA and ART on a Navigator platform (<http://www.uni-tuebingen.de/?id=8453>).*

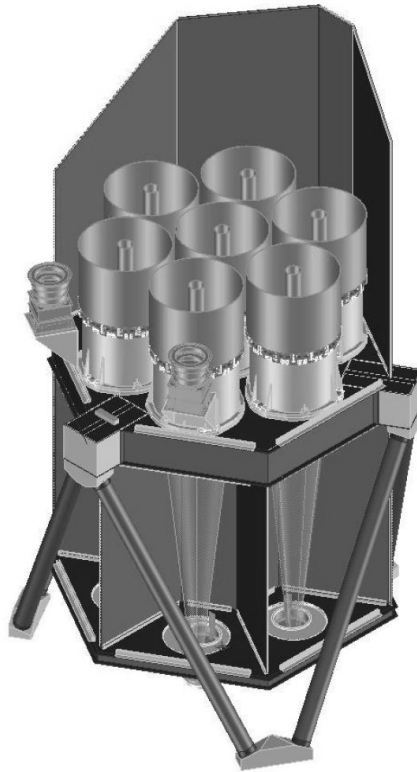


Figure 1.2: A cutaway view of eROSITA: The seven mirror modules are placed inside a hexagonal tubus (Predehl et al. 2007)

the same focal length of 1600 mm and outer diameters of 360 mm. To avoid the detection of single reflected and hence not focused photons, a so called "X-Ray baffle", a system of 54 concentric tubes, is placed in front of each mirror module. These tubes on the one side block a good fraction of the perturbing photons but also add to vignetting.

The seven mirror modules are integrated in a hexagonal sunshade and support structure (Fig. 1.2), which is connected to the spacecraft by a hexapod framework.

At the lower end of the tubus-like structure, seven pn-CCD cameras are placed, one in each telescope's focus. They have areas of $28.8 \text{ mm} \times 28.8 \text{ mm}$ with 384×384 pixels. In combination with the telescopes' optics, this results in a field of view of 1.03° . Each CCD is mounted on a ceramic printed circuit board, together with its read-out (three modified CAMEX-ASICs) and passive front-end electronics.

To reach the working temperature of -80°C , the cameras are cooled by radiator panels. These are connected to the cameras by constant and variable conductance heatpipes (CCHPs and VCHPs). With this system, regulation can be achieved at a precision of $\pm 0.5^\circ\text{C}$. No additional cold storage is needed.

The grasp, the product of effective area and field of view, can be seen in Fig. 1.3. While eROSITA's grasp exceeds that of *XMM-Newton* at energies below 2 keV, it is about three times less at high energies, due to the low ratio between focal length and aperture (f-ratio) (Predehl et al. 2010). The average angular resolution of eROSITA over the field of view is about 28 arcsec, while it is 15 arcsec on axis. This significant difference is a systematical result of the Wolter-I concept.

eROSITA will perform an all-sky-survey for four years. It will orbit Lagrange point 2 of the sun-

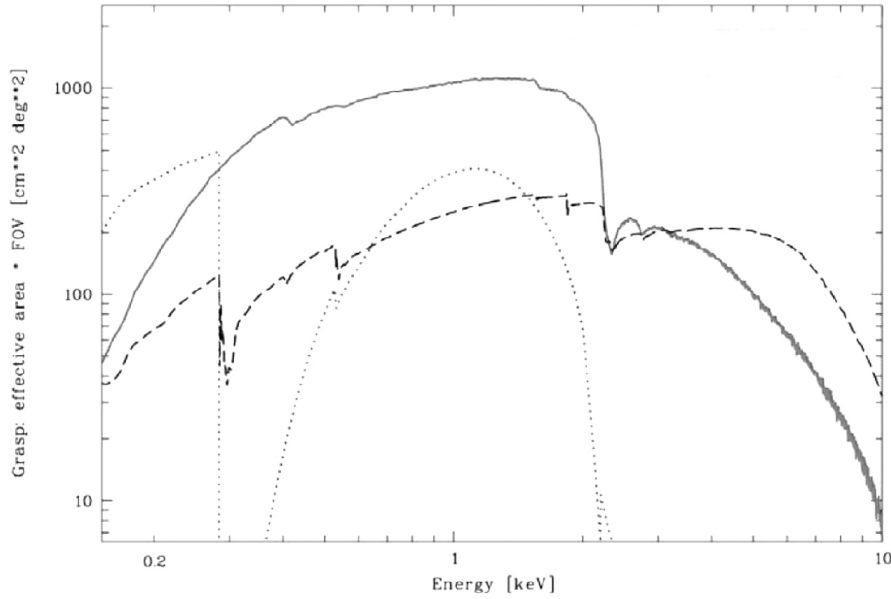


Figure 1.3: The Grasp of eROSITA, including vignetting effects (solid line), in comparison with the grasp of XMM-Newton's combined optics (dashed line) and ROSAT (dotted line). (Predehl et al. 2010)

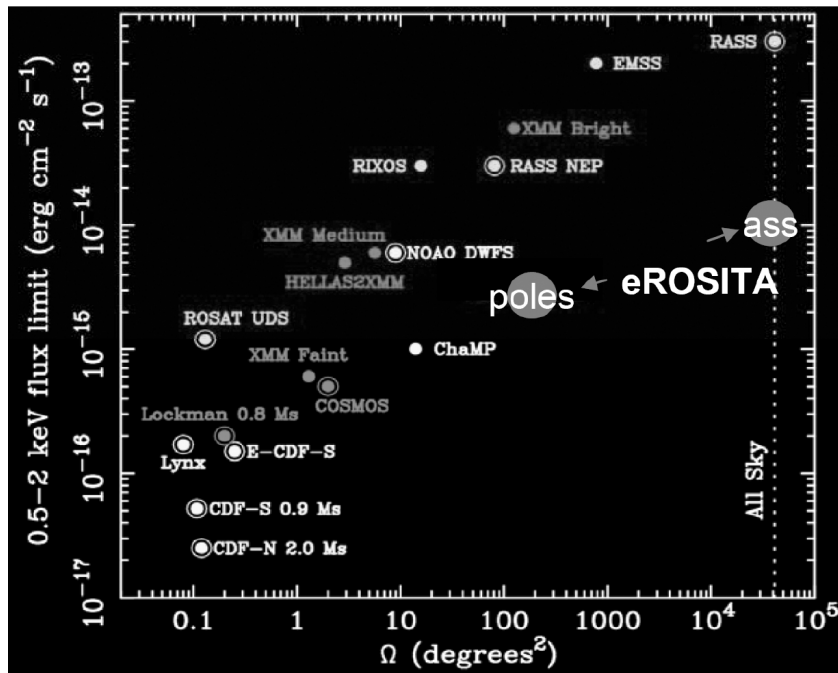


Figure 1.4: The resulting sensitivity and solid angle of the eROSITA survey (ass: all-sky-survey, poles: pole regions) as discussed in the text compared to other X-Ray-observations. (Predehl et al. 2010)

earth- system once every 180 days at an inclination of 35° with respect to the ecliptic plane. Thereby it will spin around an axis, most likely pointing towards the earth for communication. This scan strategy will result in two large areas of about 100 deg^2 around the ecliptic poles with highest exposure. Sensitivity and solid angle of this survey, compared to other X-Ray-observations, are depicted in Fig. 1.4 (Predehl et al. 2010).

During its mission eROSITA will search for answers for some of the most interesting questions of modern astrophysics. Thanks to its large collecting area and deep exposure it will be able

to study galaxy clusters and AGN at a minimum flux in the order of 10^{-14} erg s $^{-1}$ cm $^{-2}$ at the equator and up to ten times deeper at the poles in the 0.5 to 2 keV band. This will improve ROSAT data by more than one order of magnitude.

The observation of galaxy clusters is an important step for our understanding of Dark Matter and Dark Energy and a complete sample of AGN will give us essential information about the evolution of stars and black holes and so of our whole universe (Predehl et al. 2006).

1.2 Simulations for eROSITA

When the data of *Spectrum Roentgen-Gamma* is received on earth, it will be processed by the Near Real Time data Analysis software (NRTA), which is developed by a team at the Dr. Remeis-Sternwarte in Bamberg as a part of the Science Analysis Software System (SASS) for eROSITA. This software package will extract scientific information from the data stream and thereby make it possible to look for short term events and sources as, e.g., transients, and monitor the instrument's parameters for hardware problems.

As the NRTA has to be tested before the satellite gets launched, simulated data must be generated. Therefore, Christian Schmid developed a simulation which generates event files from source catalogs. It simulates the whole imaging process by using instrument specific parameters, such as Point Spread Function and the Redistribution Matrix File, to achieve realistic results.

As pointed out, source catalogs are needed for this simulation. For brighter sources, the Bright and Faint Source Catalogs of the *ROSAT* All-Sky Survey (RASS-BSC and RASS-FSC) were chosen as input. But as eROSITA will perform much deeper observations, catalogs with fainter sources, such as Active Galactic Nuclei (AGN) of the Cosmic X-Ray Background are required (Schmid 2008).

Chapter 2

The Cosmic X-Ray Background

The object of this work is to generate random object catalogs of a simulated Cosmic X-Ray Background as input for simulations of eROSITA-observations. Therefore, an introduction to the subject and its properties is given in the following chapter.

2.1 The X-Ray Background

In the middle of the last century, it became obvious that astrophysical science must not be limited to the small part of the electromagnetic spectrum which can be seen with our eyes. A lot more information about our cosmos can be discovered by building detectors for an energy range as wide as possible. This step is not as easy as it seems, because the earth's atmosphere absorbs wide parts of the spectrum, as in the X-Rays (Fig. 2.1).

With the development of the first long-range missiles during the Second World War and their further development, it became possible to transport detectors out of the dense atmosphere.

While searching for solar X-Ray-emission reflected by the moon with experiments on sounding

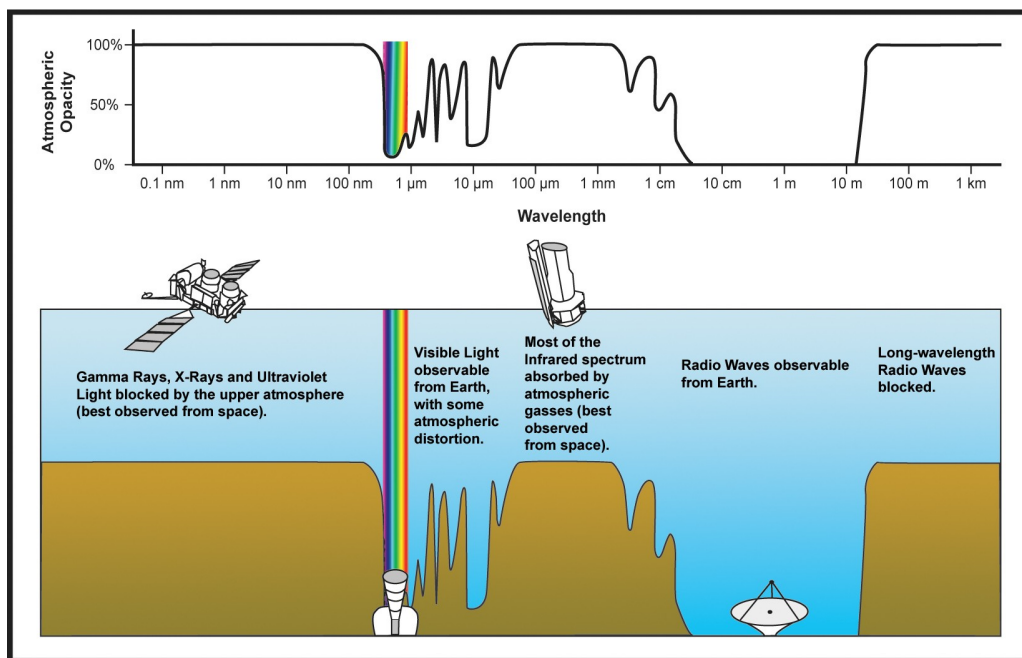


Figure 2.1: *The atmospheric opacity makes astronomical observations in wide parts of the electromagnetic spectrum impossible (<http://isc.astro.cornell.edu/~spoon/crashcourse.html>).*

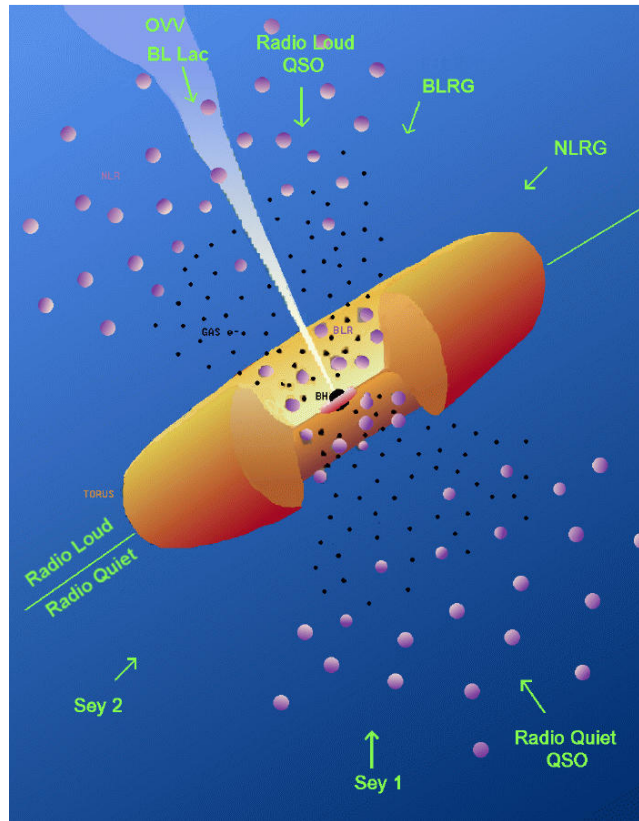


Figure 2.2: An artistic sketch of the Unified Model for AGN depicting all relevant components. The upper half shows a radio loud AGN, the lower a radio quiet AGN (<http://www.cv.nrao.edu/course/ast534/ExtraGalactic.html>).

rockets, the X-Ray Background was first detected in the early 60's (Giacconi et al. 1962). This radiation has different components: a galactic one, which is concentrated in the plane of our galaxy, and an isotropic extragalactic component. Later measurements with satellites as *ROSAT* showed that the extragalactic component of this background radiation, the “Cosmic X-Ray Background” (CXRB), can be mostly resolved into point sources, namely AGN (Hasinger 1993).

2.2 Properties of AGN

AGN are amongst the places in the universe with the highest energy density and the brightest permanent extragalactic sources in the X-Rays as seen from earth. This makes it possible to detect AGN up to very high redshifts of about 7 (Pentericci et al. 2011).

Like Urry & Padovani (1995) showed, a lot of sub-classes of high energy objects in wide frequency bands can be explained by one universal “Unified Model” of AGN as depicted in Fig.2.2.

In this model, a supermassive black hole is located in the center of its host galaxy. Its mass attracts the surrounding gaseous medium, and the preservation of angular momentum forces this material first to arrange in a thick “torus”-structure, and, more close to the center, to a thin “accretion disk”, where the angular momentum is slowly redistributed and matter eventually falls into the black hole. Here, a huge amount of energy is set free, which results in intense electromagnetic radiation up to Gamma Rays. Moreover, it is possible that the presence of strong magnetic fields forms “jets”, collimated beams of matter and radiation, which often reach fur-

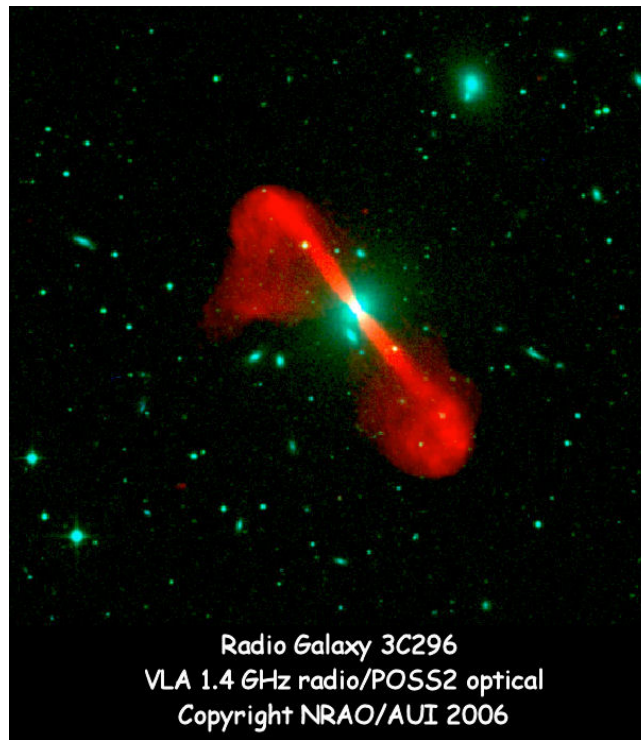


Figure 2.3: A composite picture of 3C296 shows the host galaxy and the jet which reaches far into the intergalactic medium. Optical (green): POSS2; Radio (red): VLA at 1.4 GHz. <http://www.cv.nrao.edu/~abridle/3c296digss.htm>

ther into the intergalactic space than the galactic halo and which can be observed in the radio regime as in the case of 3C296 (Fig. 2.3).

The light which is created by the accretion process has to propagate through a non-neglectable amount of energetic matter. Here, the inverse Compton process takes place, so the primary photons gain a fraction of energy from electrons with each scattering. This statistical process results in a powerlaw photon spectrum over several decades of energy. Additionally, a reflection component and iron lines which most probably originate from the ionized disk can be observed in many sources.

Furthermore, dependent on the viewing angle to the source, the central engine is more or less hidden behind the dusty torus. The matter in this structure absorbs the light proportionally to its thickness. Three main categories can be observed: unobscured sources, where the line of sight is almost perpendicular or at least in a steep angle to the accretion disk and the column density N_{H} is below 10^{21} cm^{-2} , Compton-thin obscured sources, where the line of sight pierces a small amount of the torus and N_{H} is between 10^{21} cm^{-2} and 10^{24} cm^{-2} , and Compton-thick obscured sources (N_{H} above 10^{24} cm^{-2}). The effect of varying N_{H} values on AGN spectra can be seen in Fig. 2.4 (Gilli et al. 2007).

As accretion is a dynamic process, the luminosity of AGN can vary considerably with time.

2.3 Properties of the Cosmic X-Ray Background

AGN are sources with a wide range of variety in both general and detailed properties. However, the CXRB as seen from earth consists of several millions of such sources which can not all be investigated in detail. Nevertheless, right because of the large number of objects, the CXRB as a whole can be well described by observable characteristics and distributions.

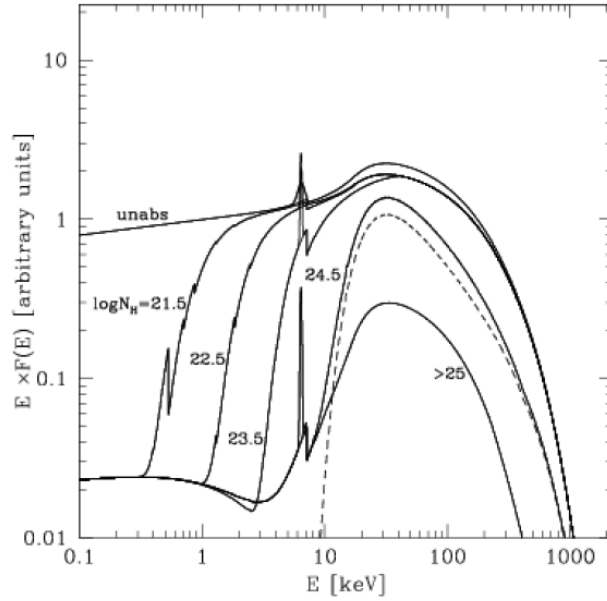


Figure 2.4: Model spectra of AGN with different column densities. (Gilli et al. 2007)

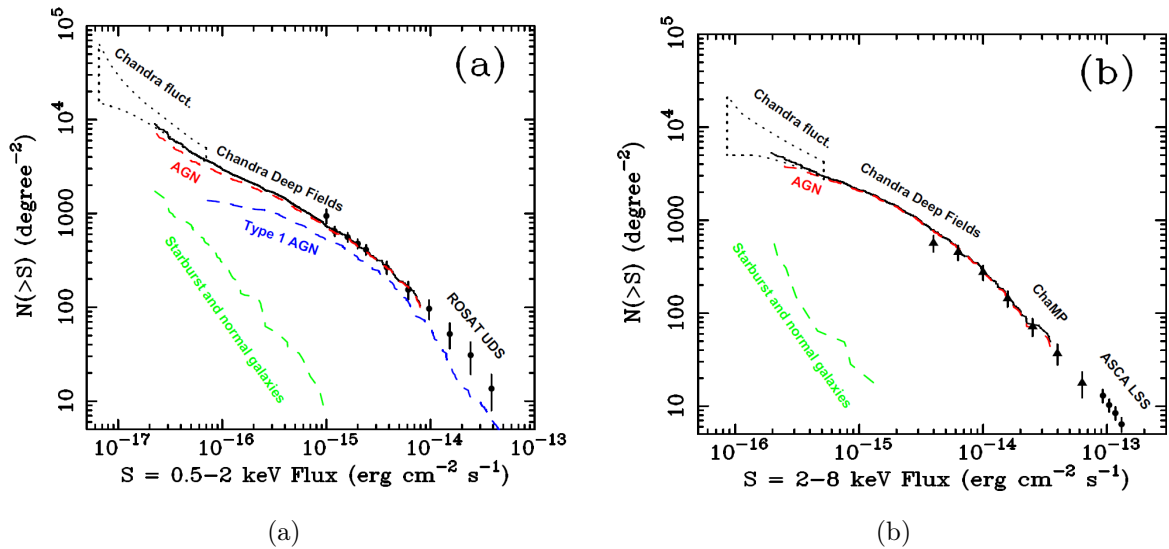


Figure 2.5: The $\log(N(>S)) - \log(S)$ plots from Brandt & Hasinger (2005) for the 0.5 – 2 keV band (a) and 2 – 10 keV band (b).

The first point to be mentioned here is a relation between the flux S and the number of detected sources with a flux higher than S . This characteristic is mostly depicted in logarithmic diagrams and is therefore called “ $\log(N(>S)) - \log(S)$ ” relation.

Surveys showed that this relation can be approximated very well by two powerlaws, one in the faint flux region and another in the brighter regime, as can be seen in Fig. 2.5 (Brandt & Hasinger 2005).

A second characteristic of the background is its total spectrum. To this, all sources contribute with their spectra, weighted with their flux. This fact alone results in a more smooth spectrum as most details average to nearly zero. Additionally, the different distances to the sources and the resulting differences in redshift wash out even more common features with narrow energy ranges, as will be seen on the example of the iron line.

The resulting spectrum as measured by *HEAO-1* and *FUKUDA* can be seen in Fig. 2.6.

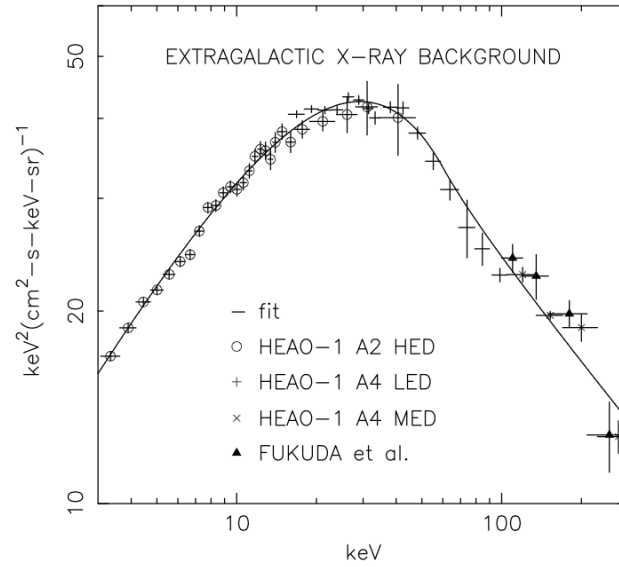


Figure 2.6: The total spectrum of the CXRB as measured by HEAO-1 and FUKUDA (Gruber et al. 1999).

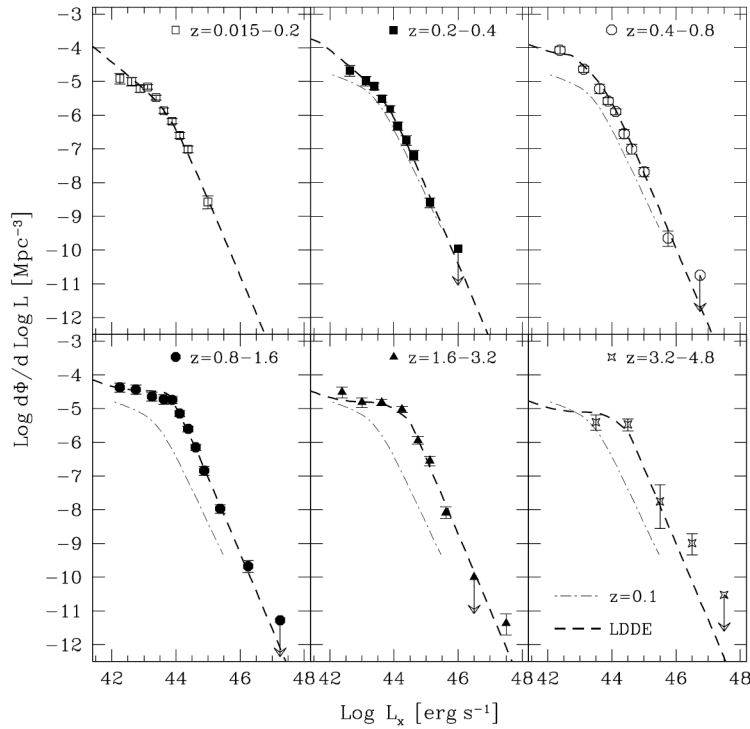


Figure 2.7: The XLF in the 0.5 – 2 keV band for six redshift intervals. The dot-dashed curve in each subplot represents the best-fit function for the $z = 0.015 - 0.2$ data (Brandt & Hasinger 2005).

A third aspect is the evolution of the X-Ray Luminosity Function (XLF). From observation data, the intrinsic or unabsorbed luminosity L_x of the sources can be calculated. This property can then be examined in relation to the sources' redshift. Such an analysis shows that the spatial density of sources with a given intrinsic luminosity varies with redshift and as a result in time. For a detailed review refer to Hasinger et al. (2005). The XLF for six redshift ranges is shown in Fig. 2.7.

Chapter 3

Simulation of the Cosmic X-Ray Background

In this chapter, the simulation of the CXRB is discussed and the output is compared to real data.

3.1 Simulation objective

As there are no high resolution widefield-maps of the CXRB in the luminosity range reached by eROSITA, a simulation is needed to fill this gap for the observation simulation. To achieve a maximum of compatibility, the output of this program is a FITS-catalog in the SIMPUT-format, as defined by Schmid et al. (2011). SIMPUT is a FITS-format, adjusted specially for easy exchange and handling of simulation output data. This is achieved by using the `simput`-library, written by Christian Schmid. The so created source list can then be combined with other catalogs containing foreground objects such as galaxy clusters and the RASS-BSC/FSC for a complete virtual X-Ray sky.

The main objective of the simulation described here is that the properties of the generated background such as the $\log(N(> S)) - \log(S)$ distribution and total spectrum match the real data as seen by *Chandra* or *XMM-Newton* by randomly setting values of position, spectral and luminosity parameters according to the measured distributions.

3.2 Program structure

The simulation as discussed in this paper operates in three steps to generate a source catalog which fulfills the requirements as set in 3.1:

1. Reading all input parameters
2. Generating the sources
3. Producing spectra

When the program is called and all necessary parameters are given correctly, it will work through these points. When it is finished, an output file in the SIMPUT-FITS-format with the specified name is returned. This file contains two data extensions:

- **SRC_CAT**: The source catalog. It contains information about source positions, luminosities and references to the spectra of each source.

- **SPEC**: The spectrum catalog. It contains all spectra which are referenced by the sources in the catalog.

The properties of the data are described in the following sections.

3.3 Parameter input

In order to enable the user to respond to changing requirements, it has to be possible to manually set most parameters in the command line. This is achieved by using the Parameter Interface Library (PIL). Part of its implementation is a parameter file, which contains the names of all free parameters, as well as information about variable types, allowed ranges and default values. When the parameters are read in, the PIL checks if they are all defined correctly in format and range using the here specified information. The parameters for this simulation are chosen to be “hidden”, which means that if the user does not specify a parameter manually in the command line when calling the program, the default value is automatically taken. This is due to the fact that most parameters won’t be changed from the preset value for a simulation run.

In the following, the free parameters are listed.

One parameter names the output catalog:

- **output_filename**: The name of the output file.

Three parameters define the geometry of the simulated area on the sky:

- **dist_max**: R ; The radius of the simulated area in degrees.
- **ref_ra**: ra_{ref} ; The right ascension of the center of the simulated area.
- **ref_dec**: dec_{ref} ; The declination of the center of the simulated area.

Two variables set the Energy reference band for the luminosity distribution and spectra:

- **Eband_low**: E_{low} ; The lower end of the simulated reference band.
- **Eband_high**: E_{high} ; The upper end of the simulated reference band.

Another eight parameters characterize the $\log(N(> S)) - \log(S)$ -distribution:

- **lower_threshold**: S_{min} ; the lowest allowed flux in the reference band.
- **upper_threshold**: S_{max} ; the highest allowed flux in the reference band.
- **source_density**: n ; The number of sources with $S \geq S_{\text{min}}$ per deg^2 .
- **powerlaw_source**: The source of the $\log(N(> S)) - \log(S)$ -powerlaw. Predefined values or additional read in with the PIL are possible.
- **powerlaw_type**¹: The type of the broken powerlaw. A smooth broken powerlaw is implemented, as is a piecewise powerlaw.
- **a1**¹: α_1 ; The index of the faint section of the $\log(N)$ - $\log(S)$ -powerlaw.
- **a2**¹: α_2 ; The index of the bright section of the $\log(N)$ - $\log(S)$ -powerlaw.
- **break**¹: S_b ; The flux of the break in the $\log(N)$ - $\log(S)$ -powerlaw.

These are all free parameters for the physical properties of the simulation. Additionally, also the values for the parameter grids of the spectral properties can be set:

- **redshift_low**: The lowest allowed value for the redshift.
- **redshift_high**: The highest allowed value for the redshift.
- **d_redshift**: The width of the linear redshift grid.
- **gamma_low**: The lowest allowed value for the photon index.
- **gamma_high**: The highest allowed value for the photon index.
- **d_gamma**: The width of the linear photon index grid.
- **nh_low**: The lowest allowed value for the logarithm of N_{H} .
- **nh_high**: The highest allowed value for the logarithm of N_{H} .
- **d_nh**: The width of the linear grid of the logarithm of N_{H} .

The function of these parameters will be discussed in 3.4.

So when the program is called, the PIL is initialized, reads the parameter values, they are printed on the screen for control and then given to the simulation functions.

3.4 Random source generation

After the parameter input is finished, the main simulation starts.

As the goal of this program is the generation of a source catalog for observation simulation input, it was tried to determine as few source-intrinsic values as possible but to constrain the model to observables. As will be seen, this leads to a number of difficulties.

First, the total source number N in the simulated area is calculated, using Equation 3.1.

$$N = n \cdot \frac{2\pi}{(\pi/180)^2} \cdot (1 - \cos(R)) \quad (3.1)$$

Then, the main loop begins, which evaluates the physical parameters of all N sources and writes them into the output file.

3.4.1 Source positions

At the beginning, every source gets two coordinates on the virtual sky, right ascension ra and declination dec . Both values are chosen randomly and independent from any other parameters, as long as they result in a position which is nearer to the reference point ($ra_{\text{ref}}, dec_{\text{ref}}$) than R . To achieve this, first a random number $rand$ between 0 and 1 is generated. The right ascension distribution is constant between 0° and 360° , so $rand$ is simply multiplied by 360° :

$$ra = rand \cdot 360^\circ \quad (3.2)$$

Because of the coordinate system, the declination has to be handled differently. The correct distribution can be derived from the dependency of the surface integral in spherical coordinates.

¹: These parameters are only read in with the PIL, if **powerlaw_source** is defined as "PIL". If **powerlaw_source** is e.g. "BrandtHasinger2005", predefined values are taken instead.

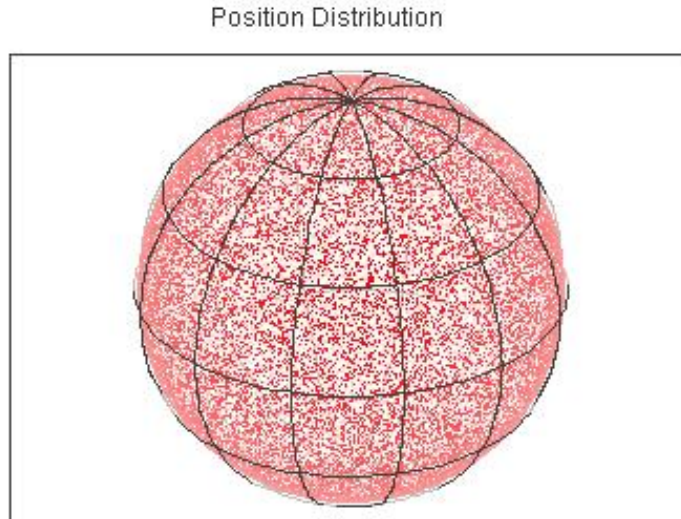


Figure 3.1: A spherical projection of an example source catalog using TOPCAT

This results in Equation 3.3. dec -values near to $\pm 90^\circ$ are less probable than values near the equator, so that the resulting source density is constant.

$$dec = \arccos(2 \cdot rand - 1) - 90^\circ \quad (3.3)$$

After the values for the position are set, the distance of the source to the reference point is calculated:

$$d = \arccos[\sin(dec) \cdot \sin(dec_{ref}) + \cos(dec) \cdot \cos(dec_{ref}) \cdot \cos(ra_{ref} - ra)] \quad (3.4)$$

If d is bigger than R , new values are generated, until d is smaller or equal to R .

To test this method, a program was written, which counts the number of sources in several areas and so recalculates the source density of the generated sky. This is done by setting arbitrary coordinates and a radius \tilde{R} . Then the distance of the center of the resulting area A to each source is calculated by using Equation 3.4. If the result is equal or smaller than the radius, the count \tilde{N} is raised by one. Afterwards, the density is calculated with Equation 3.5:

$$n = \frac{\tilde{N}}{A} = \frac{\tilde{N}}{2 \cdot \pi / (\pi/180)^2 \cdot (1 - \cos(\tilde{R}))} \quad (3.5)$$

For demonstration purpose, an example catalog with $n = 1 \text{ deg}^{-2}$ over the whole sky was generated. A first promising view of the data in a 3-dimensional projection results in Fig. 3.1.

The data was now analyzed as described above with varying declination values, for three radii: 20° , 5° and 2.5° . The result can be seen in Fig. 3.2.

At small integration radii, the calculated density strongly fluctuates, but for larger radii, it levels homogeneously to the input density, as expected. For bigger source densities like in realistic catalogs (in the order of $1 \times 10^4 \text{ deg}^{-2}$), the fluctuations will be very small.

3.4.2 Source fluxes

The second parameter to be evaluated is the flux of each source. According to (Hasinger 2008; Brandt & Hasinger 2005), a smoothly broken powerlaw is taken as distribution rule if the input

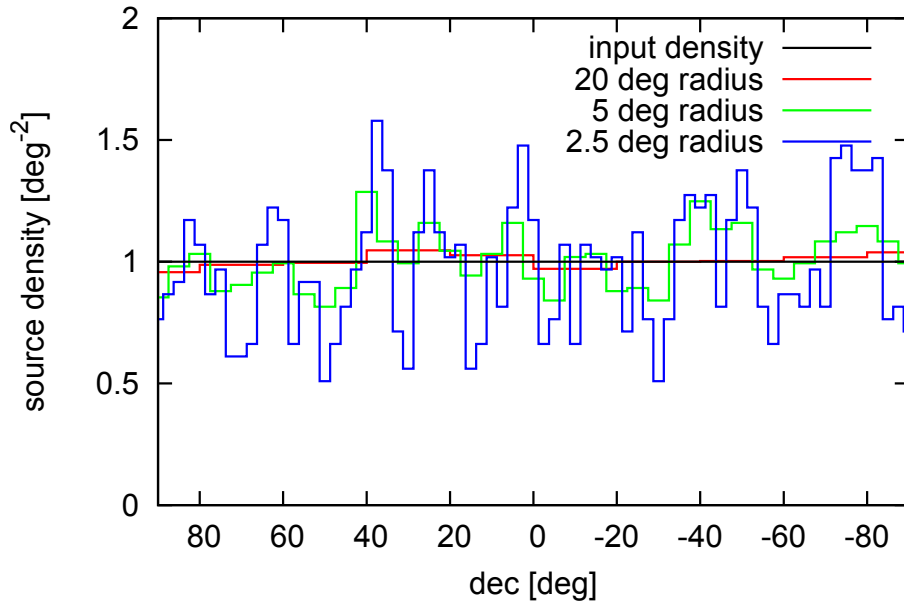


Figure 3.2: The recalculated source density n vs. declination for different integration radii

variable “powerlaw_type” is set to “smooth”. This is defined in Equation 3.6:

$$N(S) = \frac{1}{1/(N \cdot S^{\gamma_1}) + S_b^{\gamma_2 - \gamma_1}/(N \cdot S^{\gamma_2})} \quad (3.6)$$

with $\gamma_{1/2} = -(1 + \alpha_{1/2})$ (so that $\alpha_{1/2}$ actually describe the slopes of the $\log N(> S) - \log(S)$ -powerlaw).

The function is integrated numerically in the interval $[S_{\min}, S_{\max}]$ and normalized to obtain the Cumulative Distribution Function (CDF). Now a random number $rand$ between zero and one as in 3.4.1 is generated. The inverted normalized CDF is evaluated at $rand$ and the result is saved as the flux value for the source in the reference band (Gentle 2009).

Another powerlaw function, not smoothly broken, is also implemented and can be accessed with “powerlaw_type=step”. As this is an easier and not as realistic variant as the smoothly broken one it will not be discussed further.

Another program was created which evaluates the $\log N(> S) - \log(S)$ -distribution of the generated source list for several energy bands. Therefore, at first all source spectra ($F(E)$) are integrated in the band intervals. Together with the flux in the reference band, the flux in any other band (E_1, E_2) can so be calculated using Equation 3.7.

$$S_{E_1, E_2} = \frac{\int_{E_1}^{E_2} F(E) dE}{\int_{E_{\text{high}}}^{E_{\text{high}}} F(E) dE} \cdot S_{\text{ref}} \quad (3.7)$$

After the fluxes of each source in every energy band are obtained, the number of sources with $S_{\text{source}} > S$ for a fine grid in S is counted.

The resulting $\log N(> S) - \log(S)$ plot for a sample catalog with $n = 8 \times 10^3 \text{ deg}^{-2}$, $R = 2.6 \text{ deg}$, $\alpha_1 = 0.4$, $\alpha_2 = 1.6$, $S_b = 8 \times 10^{-15} \text{ erg s}^{-1} \text{ cm}^{-2}$, $S_{\min} = 1 \times 10^{-16} \text{ erg s}^{-1} \text{ cm}^{-2}$ and no upper flux limit ($S_{\max} = 2 \times 10^{-1} \text{ erg s}^{-1} \text{ cm}^{-2}$) in the reference band (2 – 10 keV) is depicted together with the input CDF in Fig. 3.3.

The consequence of this method is that if the distribution is reproduced correctly in the reference energy band (i.e. the code works and the input parameters are correct), any deviations in other bands from the real data must be caused by wrong spectral properties of the sources.

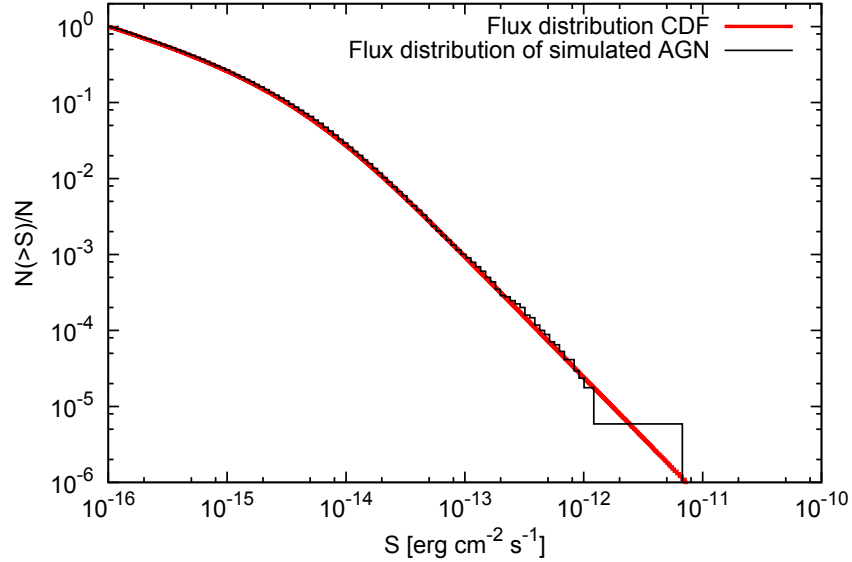


Figure 3.3: The $\log N(> S) - \log(S)$ distribution for a sample catalog renormalized to $N(> S)/N$ together with the input CDF.

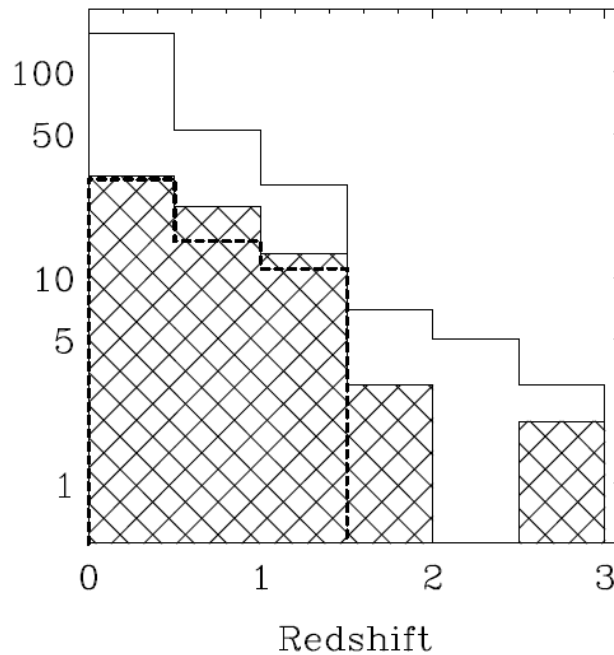


Figure 3.4: The total redshift distribution from Ueda et al. (2003) (white histogram).

3.4.3 Redshift distribution

Now that the source has a position on the sky and a brightness, the remaining coordinate - in radial direction - has to be determined. This coordinate is here defined in units of redshift (z). As described in Section 2.3, the luminosity distribution of AGN is correlated with the redshift, and so is the flux as measured on earth. For the simulation approach as described here, a correlation function between z and S would be needed, but to the date of submission such a function was not available. It was chosen to implement a flux-independent redshift distribution instead, which was taken from Ueda et al. (2003) and is shown in Fig. 3.4.

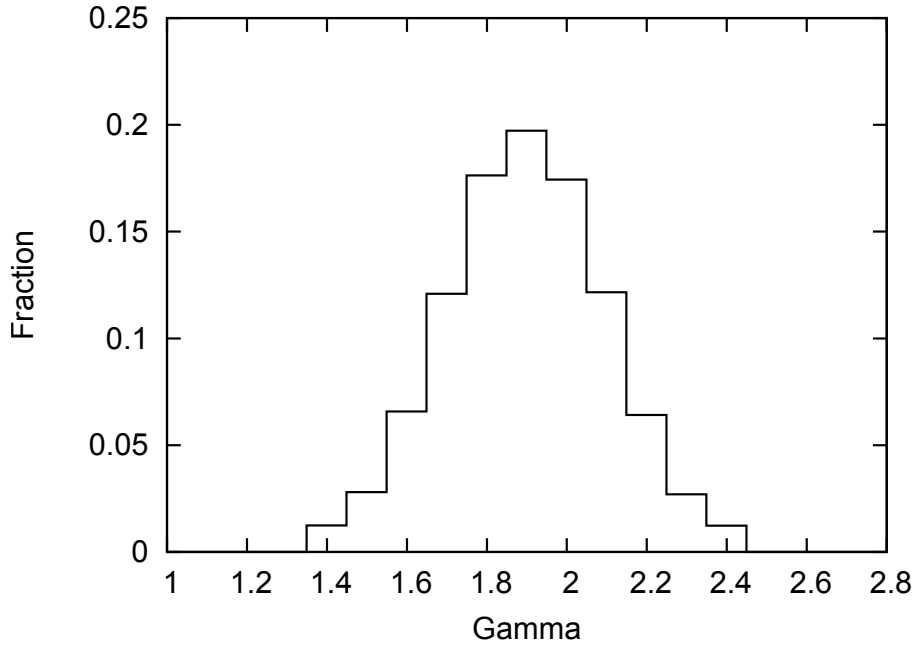


Figure 3.5: *The distribution of Γ for a sample catalog.*

3.4.4 Spectral indices

Now, the spectral properties of the sources have to be determined. The first of them is the spectral index Γ . According to Gilli et al. (2007), a Gaussian distribution with a center at $\Gamma = 1.9$ and a width of $d\Gamma = 0.2$ was assumed. This was evaluated using the GSL-random number generator for Gaussian distributions. No relation to other parameters was assumed.

For test purpose, the value of Γ can be extracted from a catalog and visualized, as done in Fig. 3.5. This plot shows a distribution as expected.

3.4.5 Column densities

The column density N_{H} of each source is dependent on its luminosity. According to Gilli et al. (2007), the number ratio between Compton thin obscured sources and unobscured sources ($N_{\text{Cthin}}/N_{\text{unobs}}$) can be calculated with Eq. 3.8

$$R(L_x) = R_S e^{-L_x/L_c} + R_Q(1 - e^{-L_x/L_c}) \quad (3.8)$$

with $R_S = 4$, $R_Q = 1$ and $L_c = 10^{43.5}$.

As also Compton thick sources exist, the factor $c = N_{\text{Cthick}}/N_{\text{Cthin}}$ is introduced. The probability of a source to be Compton thin is then given by Eq. 3.9.

$$p_{\text{Cthin}} = \frac{R(L_x)}{1 + (1 + c)R(L_x)} \quad (3.9)$$

Respectively, the probability to be Compton thick is $p_{\text{Cthick}} = c \cdot p_{\text{Cthin}}$ and to be unobscured $p_{\text{unobs}} = 1 - (p_{\text{Cthin}} + p_{\text{Cthick}})$.

As Gilli et al. (2007) chose a completely different approach for their simulation by first determining the intrinsic physical parameters of the AGN in their comoving frames and afterwards filtering the sources according to their flux dependent visibility on earth, they could use existing data for the evolution of the XLF. It is obvious that Eq. 3.8 leads to wrong results

$\log N_{\text{H}}$	$p(N_{\text{H}})$
21 – 22	0.05
22 – 23	0.35
23 – 24	0.60

Table 3.1: The probability values for N_{H} in the case of Compton thin obscuration

$\log N_{\text{H}}$	$p(N_{\text{H}})$
24.5	0.50
25.5	0.50

Table 3.2: The probability values for N_{H} in the case of Compton thick obscuration

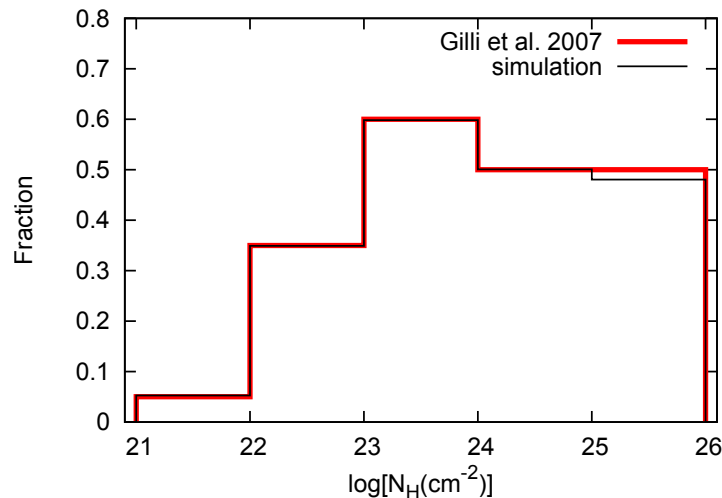


Figure 3.6: The distribution of N_{H} for obscured sources of a sample catalog together with the distribution from Gilli et al. (2007). The data was normalized so that the sum over the Compton thin sources is one.

when applied to the simulation as discussed here with luminosity independent redshift. To the time of submission, no better data was available, so a constant was chosen for $R(L_x)$, namely $R = R(L_x) = 1.6$, following the best fit for a constant intrinsic ratio between Compton thick and thin sources from Gilli et al. (2007). In Chapter 3.6, the value will be replaced.

The degree of obscuration is now determined by a random number between zero and one as described above.

If the source is unobscured, the value of N_{H} is set to 1. For the two other cases, the distribution of Gilli et al. (2007) was taken into account. Initially, the factor c was set to 1 but will also be replaced in Chapter 3.6. The probability density in the intervals between $\log N_{\text{H}} = 21, 22, 23, 24, 25$ and 26 was assumed to be constant, as the value for N_{H} later will be binned into these intervals anyways. The probabilities for the intervals were set according to Tables 3.4.5 and 3.4.5.

The actual value for N_{H} was then obtained by generating a second random number.

As previously done with Γ , the values of N_{H} can be restored from a source catalog. Fig. 3.6 shows the reconstructed distribution in comparison with the one from Gilli et al. (2007) for obscured sources.

3.4.6 Grids and source catalog

After all relevant physical parameters for a source have been evaluated, the data is prepared for storage in the source catalog (SRC_CAT).

While the parameters ra , dec and S are included in the catalog itself, the spectral parameters Γ and N_{H} as well as the redshift z are saved only indirectly as reference to the proper spectrum. As it is not efficient to generate spectra for all evaluated combinations of these parameters, they were sorted in grids defined by the free input parameters described in 3.3. These grids are linear in Γ and z and can be adjusted when calling the simulation. The only exception is the grid for N_{H} . As stated above, for the different stages of obscuration, different distributions are implemented. The grid for N_{H} so only resorts the values of Compton thin sources, as in the other cases the allowed values are already discrete. The grid hereby is linear in $\log(N_{\text{H}})$.

The now sorted grid values are combined into a name for the spectrum, in the form

$$\text{NAME}=\text{BG}[\Gamma]\text{NH}[\log(N_{\text{H}})]z[z] .$$

All values and the spectrum reference are then passed to the SIMPUT-routines which append them to the catalog in the correct form.

3.5 Generation of spectra

When all sources are evaluated and appended to the source catalog, the second FITS extension (SPEC) has to be written. This table contains spectra with all combinations of the values in the grids of the spectral parameters Γ , N_{H} and z .

As the actual process of spectrum construction is done via ISIS, every spectrum is generated in 5 steps:

1. Defining an energy grid
2. Writing a parameter file for ISIS
3. Writing a script for ISIS
4. Execute the script with ISIS
5. Storing the data in a temporary file

The energy grid is logarithmic and contains the energy values of all bin borders.

The spectral model of the simulated XRB-AGN is dominated by a reflected powerlaw with exponential cutoff at $E_{\text{Cutoff}} = 200 \text{ keV}$ and the photon index Γ . The function ‘‘pexrav’’ (Magdziarz & Zdziarski 1995) which is used for this model includes some more parameters which are set to resemble the spectra from Gilli et al. (2007) as good as possible if they are not listed directly in the paper.

In detail, these parameters are:

- `rel_refl`: the degree of reflection
- `abund`: abundance of metals
- `Fe_abund`: abundance of iron

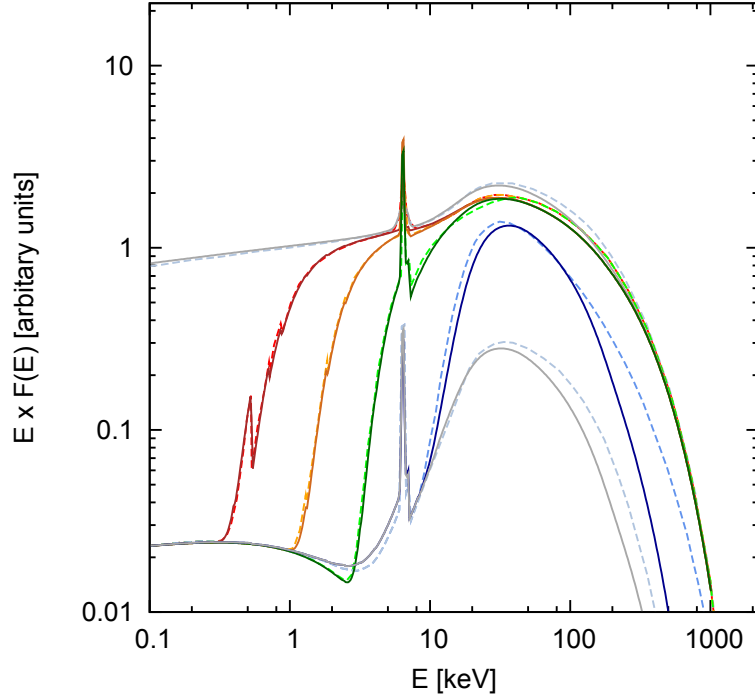


Figure 3.7: The spectra generated with ISIS for this simulation (dark, full lines) together with the spectra from Gilli et al. (2007) (bright, dashed lines). From top to bottom: $\log(N_{\text{H}}) = 0, 21.5, 22.5, 23.5, 24.5, 25.5$.

- $\cos\text{Incl}$: cosine of inclination angle

abund and Fe_abund were both set to 1 for each spectrum, and $\cos\text{Incl}$ to 0.45. rel_refl has to be changed for different values of $\log(N_{\text{H}})$: for unobscured sources, it is set to 1.3, for Compton thin spectra to 0.88 and for Compton thick spectra to -1.5 ($\log(N_{\text{H}}) = 24.5$) and -0.37 ($\log(N_{\text{H}}) = 25.5$). Thereby, negative values result in a reflection component without primary powerlaw. In the case $\log(N_{\text{H}}) = 25.5$, the column density for the absorption function was then set to zero to match the data.

The second component is another powerlaw with exponential cutoff, with the same photon index but with a cutoff energy at $E_{\text{Cutoff2}} = 3$ keV and a norm of 3% of the norm of the primary powerlaw. This component is most important for obscured sources below 1 – 10 keV.

Also reproduced is an iron line at 6.4 keV. This was implemented as Gaussian function. The width σ and equivalent width eqw vary also with degree of obscuration. For unobscured sources, σ is set to 0.4 keV and eqw to 280 eV. For obscured sources, σ is 0.1 keV and eqw varies from 280 eV ($\log(N_{\text{H}}) = 21.5$) to 2000 eV ($\log(N_{\text{H}}) = 25.5$).

A last component is another reflected powerlaw with exponential cutoff, with the same parameters as the primary one but only visible for $\log(N_{\text{H}}) > 24$ and with rel_refl set to -0.37 ($\log(N_{\text{H}}) = 24.5$) and 0.88 ($\log(N_{\text{H}}) = 25.5$).

The resulting spectra for $\log(N_{\text{H}}) = 0, 21.5, 22.5, 23.5, 24.5$ and 25.5 at $\Gamma = 1.9$ and $z = 0$ can be seen in direct comparison with the Spectra from Gilli et al. (2007) in Fig 3.7. As eROSITA is not sensitive at energies above some 10 keV, the errors of the model at highly obscured spectra at high energies can be neglected.

3.6 Comparison of the simulated XRB to real data

Now that the simulation is described, a sample output can be analyzed and compared to the real CXRB.

A catalog for a field with the same parameters as in Section 3.4.2 containing 169868 sources was generated. The resulting $\log(N(> S)) - \log(S)$ distributions in the 2 – 10 keV band (reference band) and the 0.5 – 2 keV band can be seen in Fig. 3.8. Both curves generally match the real data, with a slight difference in the 0.5 – 2 keV but a perfect fit in the reference band as expected.

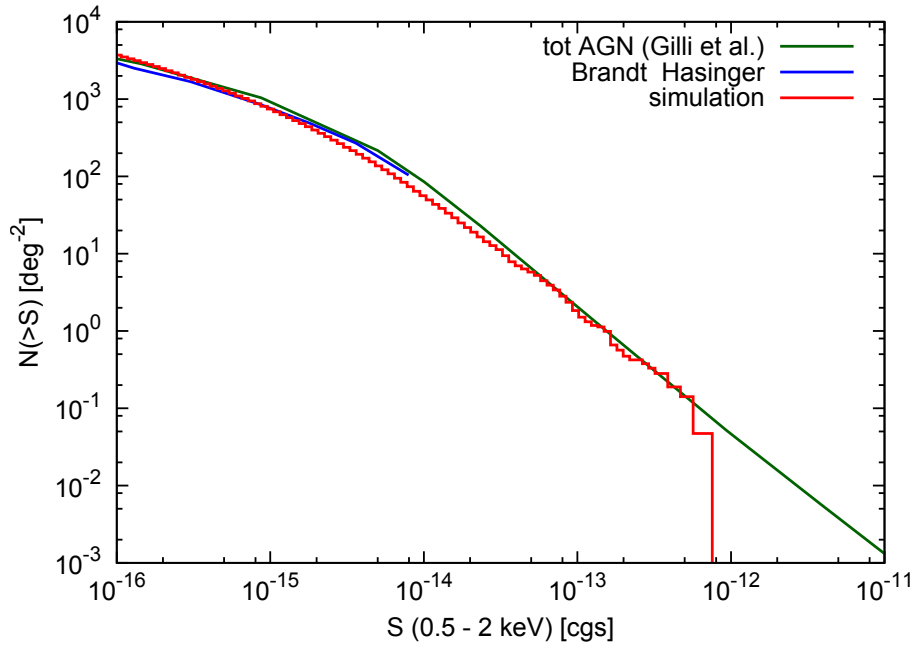
The total spectrum for the same catalog can be seen in Fig. 3.9(a). Obviously, the simulated spectrum doesn't represent the real data (in this case from *HEAO-1*) at all. A second look also shows that the ratios of the contributions of the different obscuration groups are in total disagreement with the prediction of Gilli et al. (2007). This leads to the assumption that the intrinsic ratios between the different degrees of obscuration are not qualified for this kind of approach. In fact, Gilli et al. (2007) predict a $\log(N_{\text{H}})$ -distribution with more sources in the Compton thick regime than in previous models. For the simulation as described in this paper, this may automatically lead to problems, because a large number of highly obscured sources at high distances will not be detectable due to low fluxes.

Based on the disagreement of the total spectrum to references, the ratios between the three degrees of obscuration were changed iteratively to better fit the existing data. $c = 0.07$ and $R = 1.5$ result in a better fitting spectra, as can be seen in Fig. 3.9(b). The groups of different absorption are now closer to the reference data as is the overall spectrum.

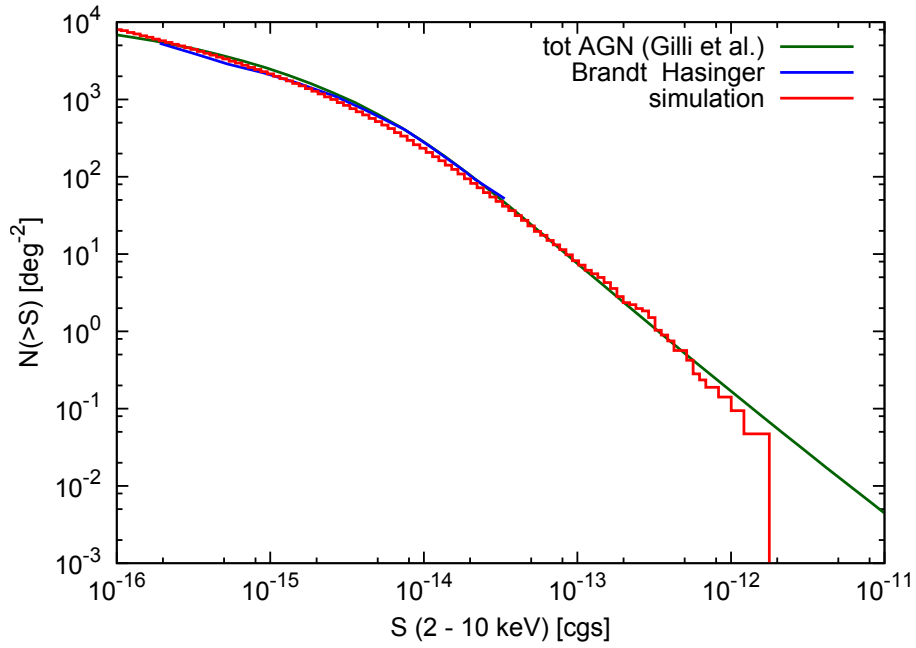
Fig. 3.10 shows the full $\log(N_{\text{H}})$ -distribution to the catalogs with the initial and the modified weights. It is obvious that the balance moved towards unobscured sources, which are detectable at greater distances and so are represented by a larger observed ratio than their total fraction.

The $\log(N(> S)) - \log(S)$ was not affected significantly from the change, as Fig. 3.11 shows.

Another simulation specific feature are the visible “forests” of iron-lines in the summed spectra. This is caused by a too wide grid for the redshift ($dz = 0.1$ in the catalogs for Fig. 3.9). A narrower grid ($dz = 0.025$) on the one side smoothes this feature as can be seen in Fig. 3.12, but also multiplies the disk space as well as the generation and calculation time.

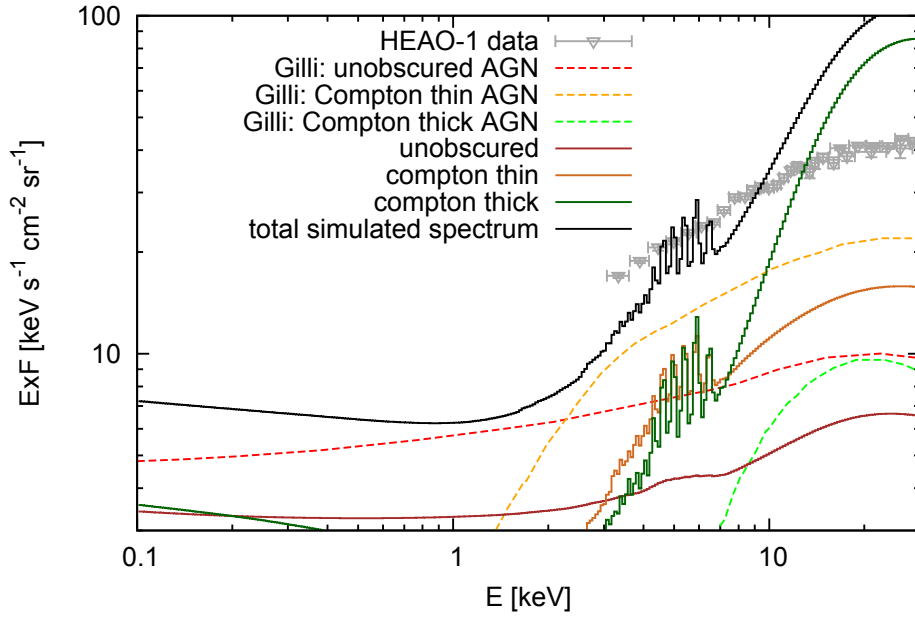


(a)

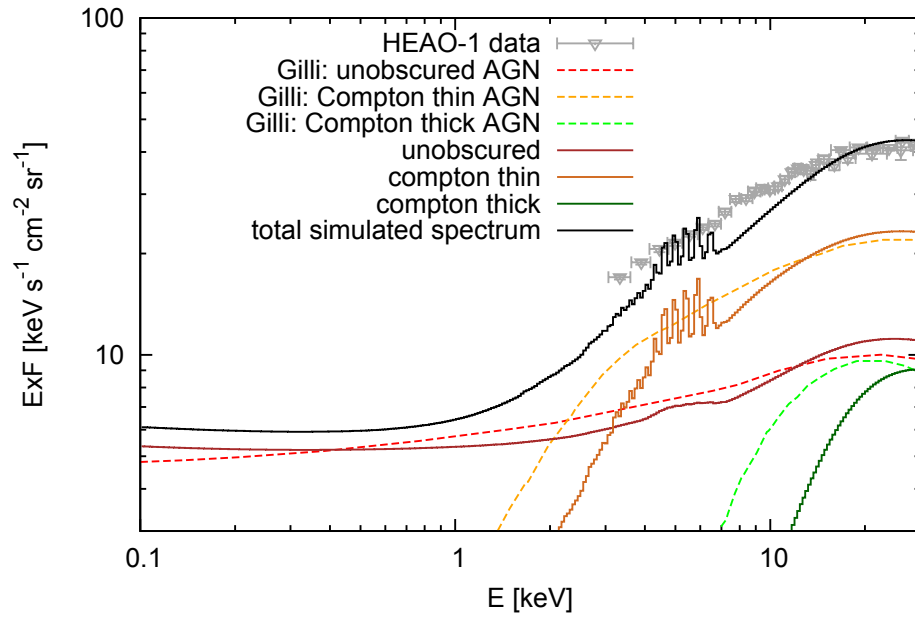


(b)

Figure 3.8: The $\log(N(>S)) - \log(S)$ -distributions in the 0.5 – 2 keV band (a) and 2 – 10 keV band (b) with $\log(N_{\text{H}})$ distribution values from Gilli et al. (2007). Simulation results are in red, the distributions from (Brandt & Hasinger 2005) and (Gilli et al. 2007) are included in blue and dark green.

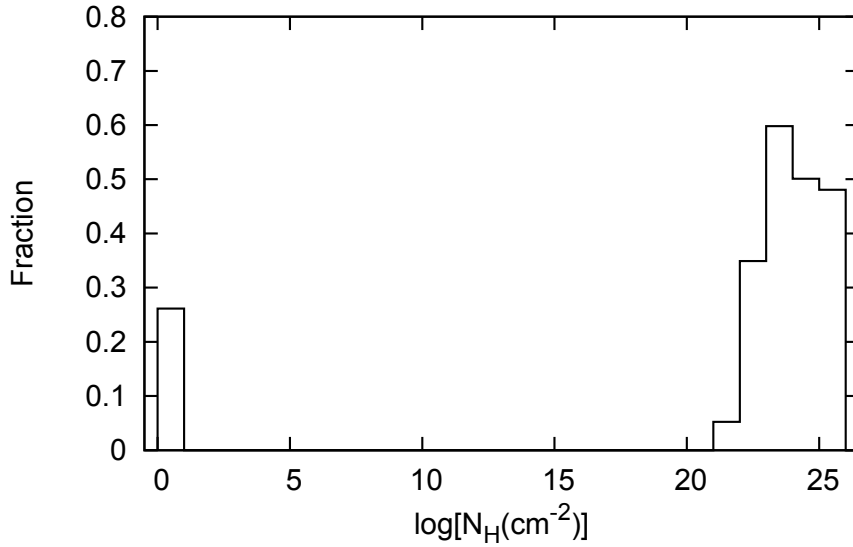


(a)

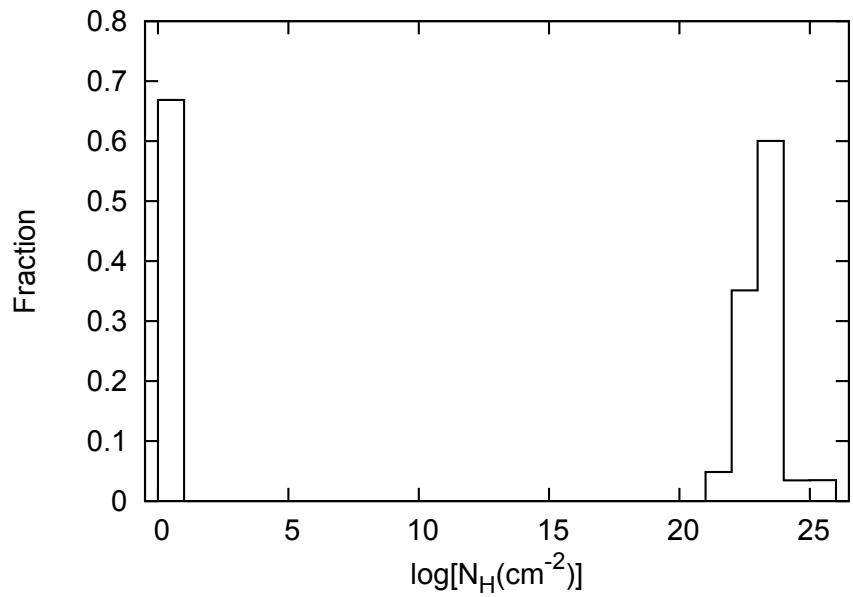


(b)

Figure 3.9: (a) The total spectrum of the simulated CXRB with $\log(N_{\text{H}})$ distribution values from Gilli et al. (2007) (black solid line). The different components of the simulated spectrum are also shown (colored solid lines), as well as the ones from Gilli et al. (2007) (dashed lines) and data from HEAO-1 (Gruber et al. 1999) (grey points). (b) Same as (a) but with modified distribution values as described in the text.

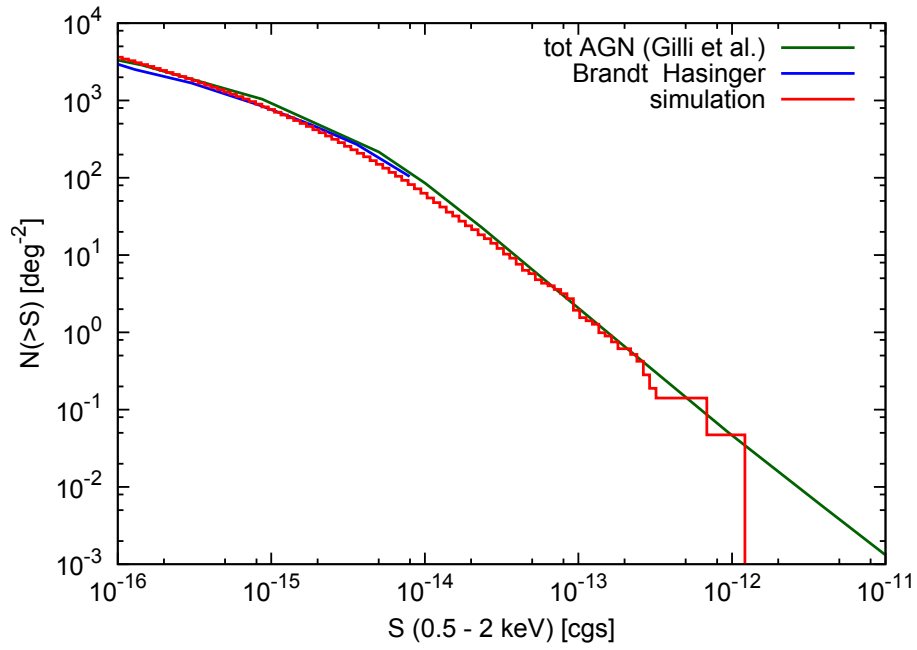


(a)

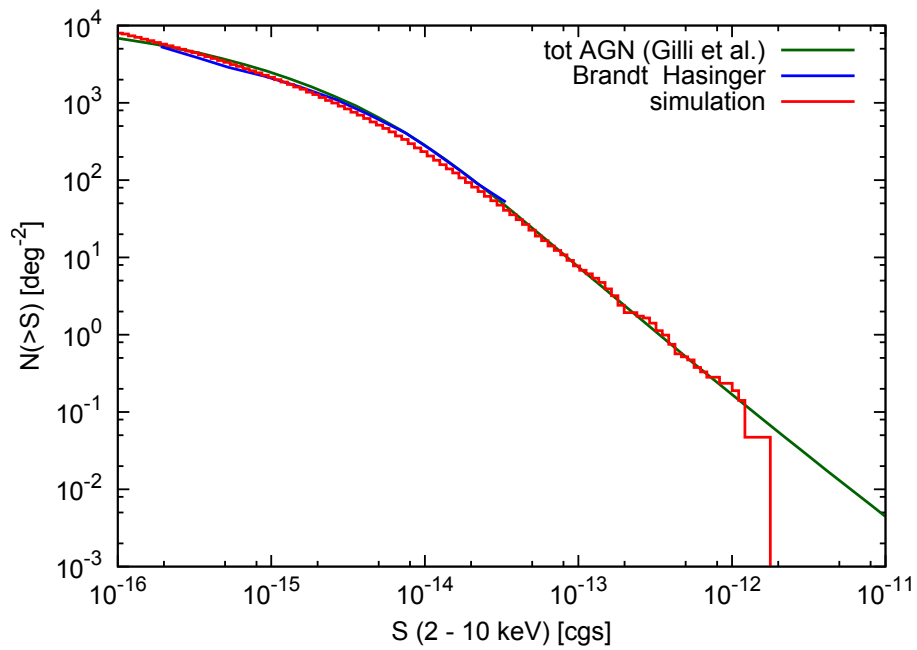


(b)

Figure 3.10: (a) The full $\log(N_{\text{H}})$ distribution with weights from Gilli et al. (2007). Unobscured sources have $\log(N_{\text{H}}) = 0$. The distribution is normalized as Fig. 3.6. (b) Same as (a) but with modified weights as discussed in the text.



(a)



(b)

Figure 3.11: Same as Fig. 3.8 but with modified $\log(N_{\text{H}})$ distribution values as discussed in the text.

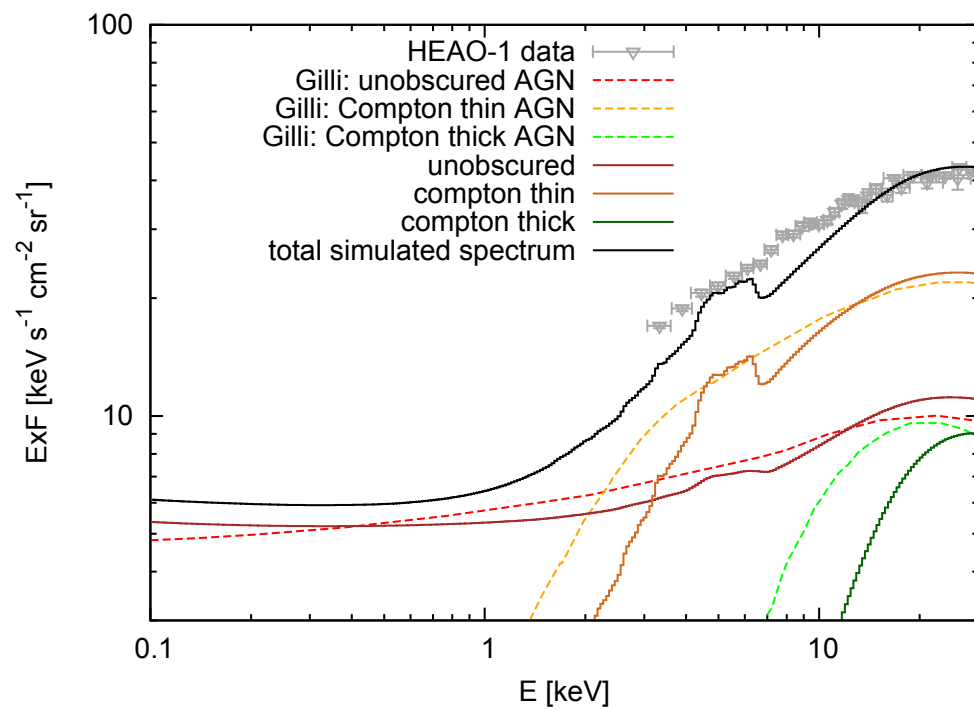


Figure 3.12: *The same as Fig. 3.9(b) but with a narrower grid in z ($dz = 0.025$)*

Chapter 4

First results of simulated observations

With a preliminary version of the program, a sample catalog containing 212335 sources dispensed over an area with 3.6° diameter has been generated by Christian Schmid for a simulated observation with eROSITA. This imitates the field of view scanning over the displayed area of the sky, with the individual stripes of the scan parallel to each other. This is similar to what will be realized on the equator during the all-sky-survey. The observation as depicted here results in a total exposure time of about 110 s. First pictures, reconstructed from the simulated event files, are presented in the following.

Fig. 4.1 shows a $3.6^\circ \times 3.6^\circ$ wide field. For this simulation run, only the AGN of the CXRB have been included. The contrast is raised significantly for this picture to identify a big number of sources.

Fig. 4.2 shows the same field, but now also simulated galaxy clusters from the authors of Borgani et al. (2004) and Roncarelli et al. (2006) are included. These are much brighter than the individual sources of the CXRB, what makes it difficult to find the faint AGN. In this picture, just the brightest sources of the simulated background can be identified visually.

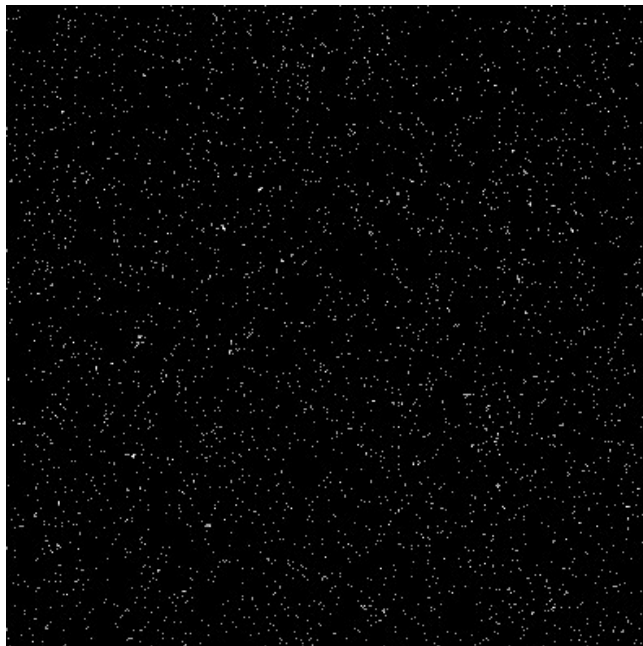


Figure 4.1: A sample picture of the observation simulation. Only CXRB sources are observed here (Picture by Christian Schmid).

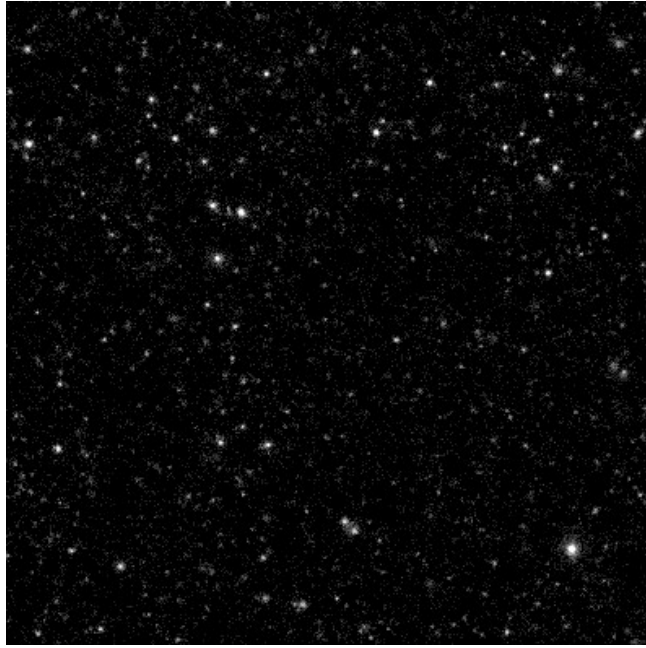


Figure 4.2: *A simulated observation of the same field as in Fig. 4.1, but also with galaxy clusters (Picture by Christian Schmid).*

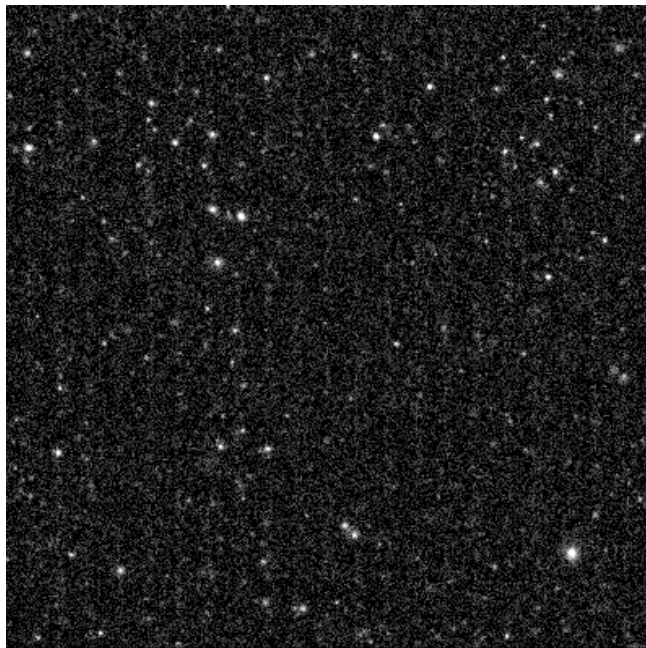


Figure 4.3: *The same as in Fig. 4.2, but now also with the Cosmic Particle Background (Picture by Christian Schmid).*

When also the Cosmic Particle Background is included, the signal to noise ratio drops significantly, as Fig. 4.3 shows. This additional kind of diffuse radiation results in a noisy pattern which can compare in flux with most sources of the XRB and consequently has direct influence on the instrument's flux limit for astronomical sources.

As these pictures are based on an older version of the simulation for the CXRB, further runs with enhanced versions will follow. Source detection analysis can determine the flux limit to which eROSITA is able to resolve these sources. Results will be discussed in future papers.

Chapter 5

Conclusions

The simulation as presented in this paper can generate source catalogs which imitate the properties of the CXRB as a whole. The flux distribution and total spectrum are reproduced well, as are the spectral properties Γ , N_{H} and the redshift z on their own. On the other side, important relations between the individual parameters are not implemented successfully. This is caused by the complexity of the physical model in interaction with the general approach of this program. As this inaccuracy may not be very important for pure observation simulations, the primary objective of this thesis is achieved.

However, the lack of these relations leads to a physically incorrect model of the source intrinsic properties and the resulting evolution of the XLF. The only way to avoid this problem with the existing data seems to be a different simulation layout, namely to simulate the correct model of AGN in their intrinsic system and afterwards to determine “what we see”. This approach will be tackled in the time after the submission of this paper. The experience which is described here will be a good foundation for this task.

Bibliography

- Borgani, S., Murante, G., Springel, V., et al. 2004, *Mon. Not. R. Astron. Soc.*, 348, 1078
- Brandt, W. N. & Hasinger, G. 2005, *Ann. Rev. Astron. & Astrophys.*, 43, 827
- Gentle, J. E. 2009, *Computational Statistics (Springer)*, 308
- Giacconi, R., Gursky, H., Paolini, F. R., & Rossi, B. B. 1962, *Physical Review Letters*, 9, 439
- Gilli, R., Comastri, A., & Hasinger, G. 2007, *Astron. & Astrophys.*, 463, 79
- Gruber, D. E., Matteson, J. L., Peterson, L. E., & Jung, G. V. 1999, *Astrophys. J.*, 520, 124
- Hasinger, G. 1993, in *Astronomical Society of the Pacific Conference Series*, Vol. 51, *Observational Cosmology*, ed. G. L. Chincarini, A. Iovino, T. Maccacaro, & D. Maccagni, 439
- Hasinger, G. 2008, *Astron. & Astrophys.*, 490, 905
- Hasinger, G., Miyaji, T., & Schmidt, M. 2005, *Astron. & Astrophys.*, 441, 417
- Magdziarz, P. & Zdziarski, A. A. 1995, *Mon. Not. R. Astron. Soc.*, 273, 837
- Pentericci, L., Fontana, A., Vanzella, E., et al. 2011, Submitted to *Astrophys. J.*
- Predehl, P., Andritschke, R., Böhringer, H., et al. 2010, in *Proc. of SPIE*, Vol. 7732, *Space Telescopes and Instrumentation 2010: Ultraviolet to Gamma Ray*, ed. M. Arnaud, S. S. Murray, & T. Takahashi, 77320U
- Predehl, P., Andritschke, R., Bornemann, W., et al. 2007, in *Proc. of SPIE*, Vol. 6686, *UV, X-Ray, and Gamma-Ray Space Instrumentation for Astronomy XV*, ed. O. H. W. Siegmund, 668617
- Predehl, P., Hasinger, G., Böhringer, H., et al. 2006, in *Proc. of SPIE*, Vol. 6266, *Space Telescopes and Instrumentation II: Ultraviolet to Gamma Ray*, 62660
- Roncarelli, M., Moscardini, L., Tozzi, P., et al. 2006, *Mon. Not. R. Astron. Soc.*, 368, 74
- Schmid, C. 2008, Diploma thesis
- Schmid, C., Smith, R., & Wilms, J. 2011, Technical report
- Ueda, Y., Akiyama, M., Ohta, K., & Miyaji, T. 2003, *Astrophys. J.*, 598, 886
- Urry, C. M. & Padovani, P. 1995, *Pub. Astron. Soc. Pacific*, 107, 803

Acknowledgements

First of all, I'd like to thank Jörn Wilms, who recommended this great subject to me and who always helped me in programming issues as well as in boosting my motivation when problems occurred.

Then I'd like to thank Christian Schmid for the good cooperation and for providing his excellent SIMPUT library which saved me a lot of time.

Furthermore, I'd like to thank Thomas Dauser, who introduced me into *ISIS*.

I also thank Ingo Kreykenbohm, who helped me a lot with C-programming and the *CFITSIO*-library, and Christoph Grossberger for all the programming (and not just programming) discussions.

My further gratitude belongs to the whole X-Ray-group of the observatory for the great ambience.

Erklärung

Hiermit bestätige ich, dass ich diese Arbeit selbstständig und nur unter Verwendung der angegebenen Hilfsmittel angefertigt habe.

Erlangen, den 01.08.2011

Thorsten Brand